Key Points:

- Snow water equivalent retrieval using X (9.6 GHz) and upper Ku band (17.2 GHz) radar observations is improved by adding lower Ku-band (13.3 GHz) data
- Passive observations are used to obtain scattering albedos, which improves the radar retrieval algorithm performance
- The resulting combined active and passive algorithm is validated against the Finnish NoSREx dataset

Correspondence to:
J. Zhu,
jiyuezhu@umich.edu

Snow Water Equivalent Retrieval Using Active and Passive Microwave Observations

Jiyue Zhu[1] (iD)**, Shurun Tan[1], Leung Tsang[1], Do-Hyuk Kang[2,3]** (iD)**, and Edward Kim[2]**

[1]Radiation Laboratory, Department of Electrical Engineering and Computer Science, The University of Michigan, Ann Arbor, MI, USA, [2]NASA Goddard Space Flight Center, Greenbelt, MD, USA, [3]ESSIC, University of Maryland, College Park, MD, USA

Abstract This paper implements a newly developed combined active and passive algorithm for the retrieval of snow water equivalent (SWE) by using three-channel active and two-channel passive observations. First, passive microwave observations at 19 and 37 GHz are used to determine the scattering albedo of snow. An *a priori* scattering albedo is obtained by averaging over time series observations. Second, 13.3 GHz is introduced to formulate a three-channel (9.6, 13.3, and 17.2 GHz) radar algorithm which reduces effects of background scattering from the snow-soil interface, and improves SWE retrieval. In the algorithm, the bicontinuous dense media radiative transfer (DMRT-Bic) is used to compute look-up tables (LUTs) of both radar backscatter and radiometer brightness temperatures (TBs) of the snowpack. To accelerate the retrieval, a parameterized model is derived from LUT by regression training, which links backscatter to the scattering albedo at 9.6 GHz or 13.3 GHz and to SWE. The volume scattering of snow is obtained by subtracting the background scattering from radar observations. SWE is then retrieved through a cost function that is guided by the *a priori* scattering albedo obtained from the passive microwave observations. The proposed algorithm, along with the active-only version, is evaluated against the Finnish Nordic Snow Radar Experiment (NoSREx) data set measured in 2009–2013. The combined active-passive algorithm achieves root mean square errors (RSME) less than 27 mm and correlation coefficients above 0.68 for 2009–2010, RMSE less than 21 mm and correlation above 0.85 for 2010–2011, and RMSE less than 40 mm and correlation above 0.38 for 2012–2013.

1. Introduction

Recent climate change has significantly altered cold land hydrological cycles, where the freshwater is highly dependent upon the presence of the snow and ice in high altitude and latitude regions (Ficke et al., 2007; Hall et al., 2008; Hauer et al., 1997; Heino et al., 2009). Terrestrial seasonal snow has been a critically important water source for water-stressed regions, providing a large fraction of the freshwater to towns in arid and semi-arid climate zones in this globally changing era (Staudinger et al., 2014). Seasonal snow is one of the most vulnerable hydrologic elements in the terrestrial water cycle (Sturm et al., 2017). Monitoring the amount of the seasonal snow in a global scale remains a challenge. Improving the estimation of terrestrial snow water equivalent (SWE) is essential to understanding cold land hydrological processes (A. T. C. Chang et al., 1987; Kelly et al., 2003; Rott et al., 2010). Several efforts have been made to improve our understanding through the use of remote sensing techniques such as passive microwave sensing (Kelly et al., 2003; Pan et al., 2017; Pulliainen & Hallikainen, 2001; Saberi et al., 2020), active microwave sensing (Cline et al., 2003; Kim et al., 2017; Lievens et al., 2019; Rott et al., 2010), lidar altimetry (Broxton et al., 2019), and signal of opportunities (Shah et al., 2017). Compared with other remote sensing and microwave techniques, the advantages of active microwave (radar) observation include high spatial resolution and the ability to penetrate clouds (Lievens et al., 2019; National Research Council, 2007; Pettinato et al., 2013; Rott et al., 2010). SWE retrieval from radar observations relies on the volume scattering of snow, which tends to increase with SWE for dry snow (W. Chang et al., 2014; Lievens et al., 2019; Tan et al., 2015; Xu et al., 2012). However, single-parameter SWE retrieval is challenging because radar backscatter is a function of several other parameters, including snow depth, snow grain size, snow density, snow stratigraphy, snow wetness, and soil/vegetation conditions (Shi & Dozier, 2000; Thompson & Kelly, 2019). Several combinations of parameters can produce the same total backscatter and generate a non-unique retrieval (King et al., 2018). Thus, *a priori* information of the parameters and the use of complementary sensors to constrain these snow parameters can improve

the accuracy of retrieved SWE based on radar observations and thereby improve our understanding of processes within snowpacks that control the persistence of seasonal snow in both the horizontal and vertical dimensions, as well as melt onset and speed. These parameters are at the heart of determining when and where seasonal snow exists, and when and how fast it will melt—parameters of particular relevance to both hydrometeorolgical and hydroclimatological science and societal applications.

Multiple studies have applied radar measurements to the retrieval of snow physical properties. Empirical inverse models were proposed in pioneering studies (Drinkwater et al., 2001; Ulaby & Stiles, 1980) that are straightforward but unsuited for all snow types—for example, ephemeral, prairie, maritime, and mountain snow, etc (Sturm et al., 1995). To cope with non-uniqueness in radar signatures, investigators applied multiple channel measurements to determine multiple snow parameters (Rott et al., 2010; Shi & Dozier, 2000). These foundational studies set the stage for more recent studies that have derived a SWE retrieval algorithm based on 10 and 17 GHz radar observations using vertical co-polarization (VV) (Cui et al., 2016; Zhu et al., 2018).

Radar observations of snow consist of two contributions: (a) volume scattering from the snowpack, which provides the SWE information and (b) background scattering from the underlying soil and vegetation, which cause uncertainties in the SWE retrieval (Shi & Dozier, 2000; Xu et al., 2012). The two biggest issues for radar SWE retrieval relate directly to these two contributions: obtaining *a priori* information to constrain the SWE retrieval from the volume scattering and eliminating the effects of background scattering from the soil.

A priori information for estimates of grain size or scattering albedo ω of snow is also important to implement an accurate SWE retrieval (Cui et al., 2016; Rott et al., 2010; Xiong & Shi, 2017; Zhu et al., 2018). The underlying physics of the non-unique solutions state that different snow microstructure configurations can have similar backscatter responses but distinct SWE (King et al., 2018; Tsang et al., 2004). *A priori* information can be obtained from co-located field stations or historical ground measurement data (Cui et al., 2016; Rott et al., 2010; Zhu et al., 2018). In some studies, snow physical models were applied to provide *a priori* information (Xiong & Shi, 2017). Lemmetyinen et al. (2018) first proposed the retrieval of the effective correlation length of snow with passive observations and in situ snow depth measurements. The derived correlation length then served as *a priori* information to parameterize the SWE retrieval with radar observations. The expanded Microwave Emission Model for Layered Snowpacks (MEMLS3&a) has been used to simulate both the backscatter and TB of snow (Proksch et al., 2015).

Some studies (Drinkwater et al., 2001) considered the background scattering contribution to be negligible when compared with the volume scattering from snow. In other studies, the ground was simply modeled as bare soil (Shi & Dozier, 2000; Zhu et al., 2018). Shi and Dozier (2000) applied L-band radar observations to retrieve soil parameters and used them to calculate background scattering. A second method applied radar observations just before snowfall or with only thin snow as background scattering (Cui et al., 2016; Rott et al., 2010). This method works in the case that soil conditions remain reasonably similar during the entire winter, otherwise the SWE retrieval accuracy will be impacted. These studies partially address background scattering, but uncertainty of the acquired background scattering remains potentially significant to overall SWE retrieval accuracy.

Zhu et al. (2018) developed a SWE retrieval algorithm that used 10 and 17 GHz VV radar observations. The algorithm proved its effectiveness in the validation of three sets of airborne SnowSAR data including the 2011 and 2012 campaigns in Finland (W. Chang et al., 2014; Meta et al., 2012) and the 2013 campaign in Canada (King et al., 2018), which achieved an RSME below 30 mm of SWE and a correlation coefficient above 0.64. Nevertheless, there are two limitations to this radar retrieval algorithm. Due to the absence of ground parameter measurements, in situ snow measurements and co-located radar observations were used to determine background scattering, and the background scattering values were not validated. Second, *a priori* scattering albedo ω was obtained by in situ measurements; however, in a satellite mission, it is not possible to obtain global in situ measurements for the scattering albedo.

In this paper, we focus our studies on overcoming these two limitations. The objectives are to:

1. Add a third frequency (13 GHz) to the original dual-frequency (10 and 17 GHz) radar retrieval algorithm to reduce uncertainties caused by the background scattering.

2. Determine *a priori* ω by applying only passive observations. *a priori* estimates are then used to initialize the radar (active) retrieval algorithm, making the method a combined active and passive algorithm.

Utilizing 13 and 17 GHz for SWE retrieval has been proposed for the Terrestrial Snow Measurement Mission (TSMM) from the Canadian Space Agency (CSA) (Derksen et al., 2018). In Figure 7 of Section 3.3, this paper shows two advantages of including the 13 GHz channel. The first is increased total sensitivity to SWE by adding a second frequency with more sensitivity (steeper slope) than at 10 GHz. The second is additional information to help minimize the impact of the background contribution since we now have a second frequency that has a stronger absolute backscatter than that at 10 GHz.

In this paper, we adopt a strategy of estimating *a priori* values from passive observations of 19 and 37 GHz. However, *a priori* information is determined purely by matching passive observations with the DMRT-Bic LUTs. There is no in situ measurement involved in this procedure. In addition, *a priori* estimates are characterized by a different parameter: the scattering albedo $\omega = \kappa_s/\kappa_e$ that represents the fraction of extinction due to scattering, where κ_s and κ_e are the scattering and extinction coefficients of the snowpack, respectively. The scattering albedo directly quantifies the scattering efficiency of the snow microstructure (grain size, snow aggregation, and other parameters) and is directly related to backscatter in DMRT theory. Higher scattering efficiency of snow is typically associated with a larger albedo. In the algorithm, the DMRT-Bic model is applied for predictions of the backscatter and TB of snow (Tan et al., 2015).

The organization of this paper is as follows: In Section 2, we describe the Finnish NoSREx data sets. In Section 3, we propose the parameterized model of DMRT-Bic for 13 GHz backscatter and generate the passive LUT for 19 and 37 GHz. In Section 4, we describe the combined active and passive retrieval algorithm. In Section 5, we evaluate the combined active and passive algorithm with the NoSREx data set. We first compare the retrieval with different frequency combinations and discuss the performance. Next, we compare the active/passive retrieval with the active-only retrieval. The background effects and accuracy of the scattering albedo retrieval from passive observations are also discussed.

2. Data

The Finnish NoSREx data set (Lemmetyinen et al., 2016) collected by the Finnish Meteorological Institute (FMI) is used to evaluate the algorithm in the paper. The NoSREx campaigns were initially performed for four successive winters 2009–2013 at the Arctic Research Center (67.3618°N, 26.6338°E) in Sodankylä, northern Finland. The site was chosen in a clear area within the spruce forest which is a typical boreal forest landscape. There is mainly short and small vegetation, such as lichen and heather, covering the area. All the short trees and bushes were removed before the snowfall each year, as shown in Figure 1. According to Lemmetyinen et al. (2016), based on a 30-year average, the soil starts freezing at the end of October, reaches maximum frost depth around early April and then thaws in the middle of May. Regarding snow conditions over 30 years, seasonal snow cover starts at the end of October and the maximum SWE occurs in April with a mean of 186.5 and 41.9 mm standard deviation. The average snowmelt-onset date is May 9.

Both active and passive microwave instruments were installed on tower platforms. The locations of sensors are shown in Figure 1. The active measurements were provided by SnowScat, a scatterometer operating at 10.2, 13.3, and 16.7 GHz (X- to Ku-band) with full polarization. The SnowScat scanned over both elevation (30°, 40°, 50°, and 60°) and azimuth angles (17 angles between −62° and 34° are scanned). Backscatter was averaged over azimuth angles. The passive measurements were collected by the SodRad which is a radiometer operating from 10.65, 18.7, 36.5, and 90 GHz (X- to W-band). Radiometer observations were made at elevation angles between 30° and 70° with a 5° increment. Both backscatter and TB measurements were collected every 3 h (2009–2010) or 4 h (2010–2013). In Figures 2a–2d, time series backscatter of all three frequencies and TB of 18.7 and 36.5 GHz at 40° elevation angle are shown, respectively.

Two kinds of co-located in situ measurements were included: manual snowpit measurements and automated snow measurements. The snowpit measurements were performed weekly 10–20 m from the footprints of the microwave sensors. Consecutive pits were made 0.5–1 m away from the previous pits. In this study, the manual measurements of SWE, snow depth, density profiles, and grain size profiles were used. The snow density profile was measured with a 250 cm^3 manual cutter and scale. The estimation of snow grain size

Figure 1. Illustration of the NoSREx campaign ground measurements system. The background picture is from Lemmetyinen et al. (2016).

was taken from visual macro-photography against a 1 mm grid. There were 81 snowpits from October 2009 to May 2010, 31 snowpits from October 2010 to May 2011, 23 snowpits from November 2011 to May 2012 and 32 snowpits from October 2012 to May 2013 (Lemmetyinen et al., 2016). There were also several automated instruments installed near the SodRad footprint to collect observations of SWE, snow depth, air and soil temperature, as well as soil moisture, which were obtained every 10 min. Snow depth was measured by an acoustic sensor and SWE was taken directly from the Gamma Water Instrument (GWI) (Lemmetyinen et al., 2016). There were some irregular values in SWE from GWI (some measurements deviate from the average) for all the seasons. These variabilities in measured SWE are errors of the automated instruments, which was confirmed by the manual snowpit measurements and studies of Lemmetyinen et al. (2016) and Lemmetyinen et al. (2018). In this paper, the basic assumption is that the snowpack was cold and dry with no liquid water present. Efforts were therefore made to center the observations on periods of dry snow accumulation. The data were chosen from the start of snow accumulation to the SWE peak during which both backscatter and TB data are available. Therefore, the study periods of December 15, 2009 to March 29, 2010, November 5, 2010 to March 13, 2011, and November 27, 2012 to April 12, 2013 were selected. Data from the 3rd year are not used because of instrument malfunction (described in Leinss et al., 2015) and the lack of observations during the dry snow season. The automated sensors and snowpit locations are shown in Figure 1. In Figures 2a–2d, time series SWE, air and soil temperature are illustrated in the bottom figures, respectively. In Figure 3, the evolution of snow stratigraphy is illustrated for 2010–2011. Considering the effects of grain size on scattering, the snowpack is separated into two layers by grain type. The layers with new and rounded grains compose the top layer and the layers with faceted grains is treated as the bottom layer (Lemmetyinen et al., 2015).
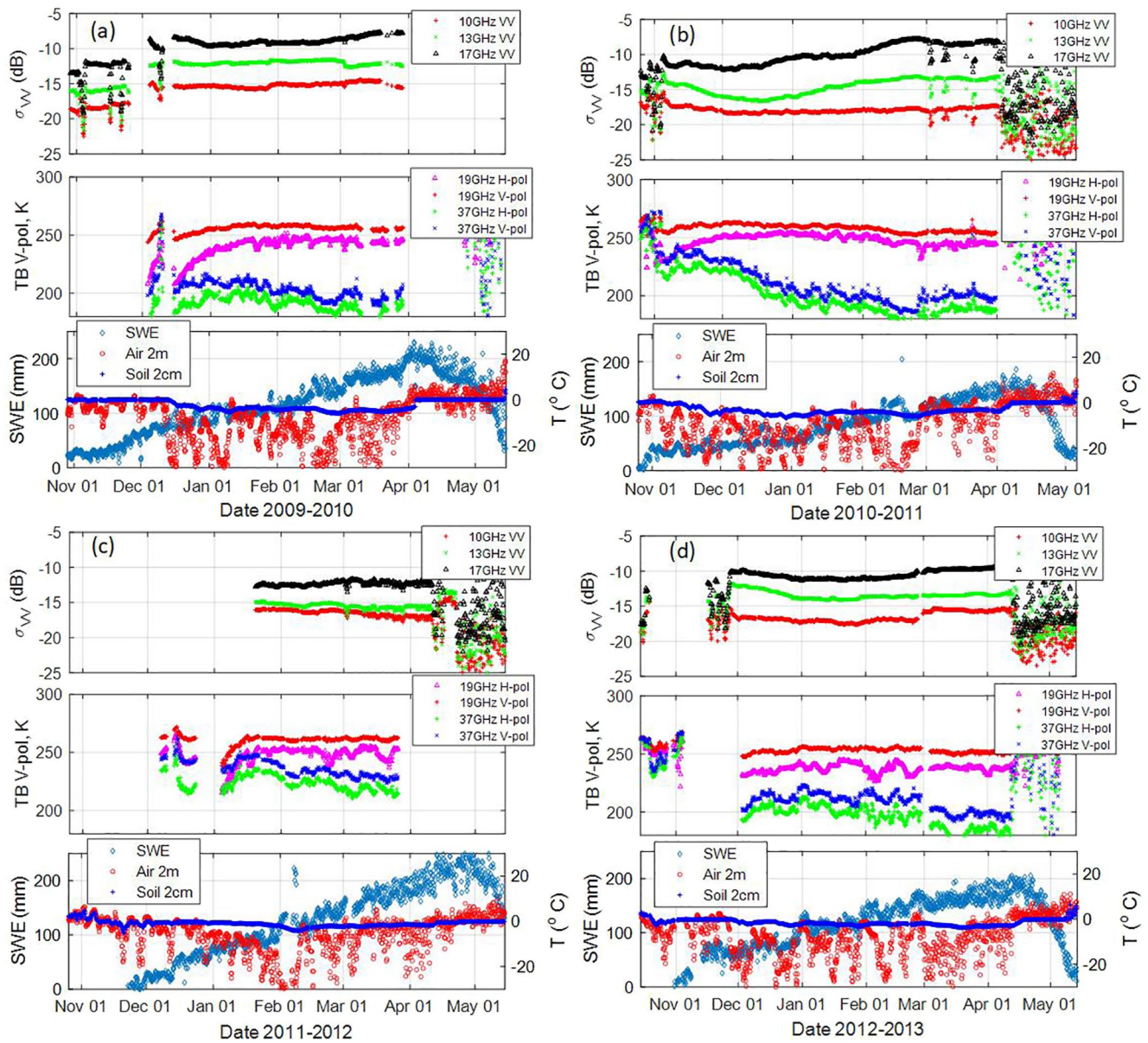
Figure 2. (a–d) Data summary of the NoSREx campaigns for 2009–2013. From top to bottom, each figure contains: the first panel is the vertically co-polarized backscatter at 10.2, 13.3, and 16.7 GHz with 40° elevation angle. The second panel is the TB at 19 and 37 GHz with 40° elevation angle; The third panel is snow water equivalent (SWE), air (at 2 m height) and soil (2 cm below soil surface) temperature measurements from automated instruments. This figure was modified from Lemmetyinen et al. (2016).

Figure 2b illustrates that 2010–2011 is the year in which the continuous backscatter and TB data from snow-free to snow melt-off are available. In other years, there were data gaps due to instrument malfunctions and installation delays (Lemmetyinen et al., 2016). In the early snow season, there were several sudden drops in backscatter which were caused by the snow melting and refreezing. This is supported by two indications: the air temperature went above and below zero during this period, and the TB data also shows several peaks at the same time--indicating episodes of high TB ~273 K. Under such conditions, wet snow can exist at or near the surface, and the snow behaves like a blackbody with low scattering. Similar phenomena are also more apparent around April 1, 2011, which is the beginning of the snow melting season. It is interesting to note that during 2009–2011 (Figures 2a and 2b) and 2012–2013 (Figure 2d) the backscatter gradually decreased after an initial increase. This was more apparent at 13.3 and 16.7 GHz than at 10.2 GHz indicating the change was dominated by changes in snow volume scattering (Lemmetyinen et al., 2016). As
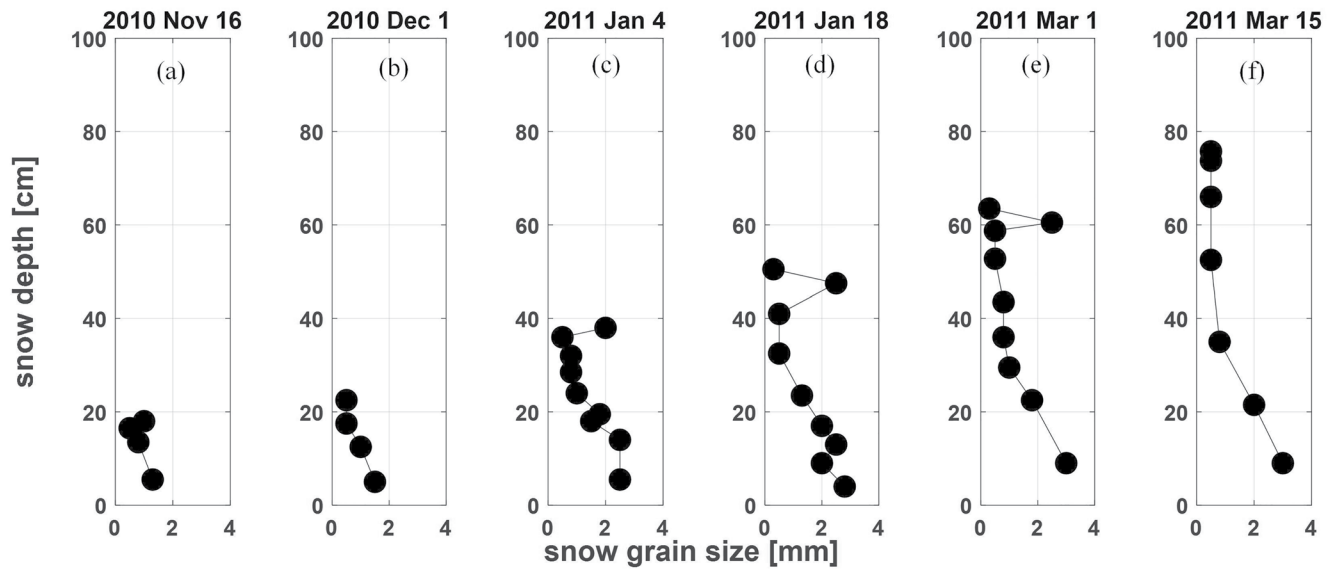
Figure 3. The time series snow stratigraphy measurements for the winter season of 2010–2011. The snowpit measurement dates are (a) November 16, 2010, (b) December 1, 2010, (c) January 4, 2011, (d) January 18, 2011, (e) March 1, 2011, and (f) March 15, 2011.

described by Lemmetyinen et al. (2016) and indicated by the early season grain size measurements (Figures 3a and 3b), the initial increase in backscatter was caused by formation of crust structures (grain size ~1 mm) in the surface of the top layer due to the melting events. The crust structures then gradually relaxed and the grain size in the top layer decreased corresponding to the decrease of backscatter. Meanwhile, the bottom layer grain size was almost constant (Figure 4b of Lemmetyinen et al. [2015]; Lemmetyinen et al. [2016]). Based on Rayleigh scattering theory, volume scattering is proportional to the third power of grain size while only linearly proportional to SWE (Tsang et al., 2004). Therefore, the change of grain size in the top layer dominated backscatter change in the early season. After that, backscatter increased with snow evolution to the more typical snow in the late season (Lemmetyinen et al., 2016). During the typical dry snow season, the backscatter at 10.2 GHz kept stable with little increase with SWE and even showed a gradually decreasing signature in 2011–2012, while backscatter at 13.3 and 16.7 GHz showed some increase until March 1 in 2009–2011 and 2012–2013 and no increase in 2011–2012. After March 1, the backscatter of 13.3 and 16.7 GHz did not increase in 2010–2011 and 2012–2013 which may be attributed to the decrease of the top layer grain size as indicated by Figures 3e and 3f. The TB measurements indicated similar effects caused by the evolution of the snowpack.

3. Methods

As illustrated in Figure 4, the retrieval method consists of four parts: the parameterized forward model derived from the DMRT-Bic LUT for predictions of snow volume scattering, the subtraction of the background scattering, the estimation of *a priori* scattering albedo $\bar{\omega}$ from passive observations, and the SWE retrieval algorithm based on three-channel (10, 13, and 17 GHz) radar observations. In the retrieval algorithm, we first obtain the volume scattering component of snow by substracting the background scattering from the total radar observation. Then, the scattering albedo ω is estimated by using a cost function to find the minimum difference between the passive observation and the passive LUT. *A priori* $\bar{\omega}$ is computed by averaging all the ω. With the obtained volume scattering component and *a priori* $\bar{\omega}$, we run the retrieval algorithm with the support of the parameterized forward model to determine SWE.

3.1. Forward Model

Figure 5 provides a flow chart of LUT generation and regression training for the parameterized DMRT-Bic model. We first apply the DMRT-Bic model to calculate backscatter (W. Chang et al., 2014; Tan et al., 2015)
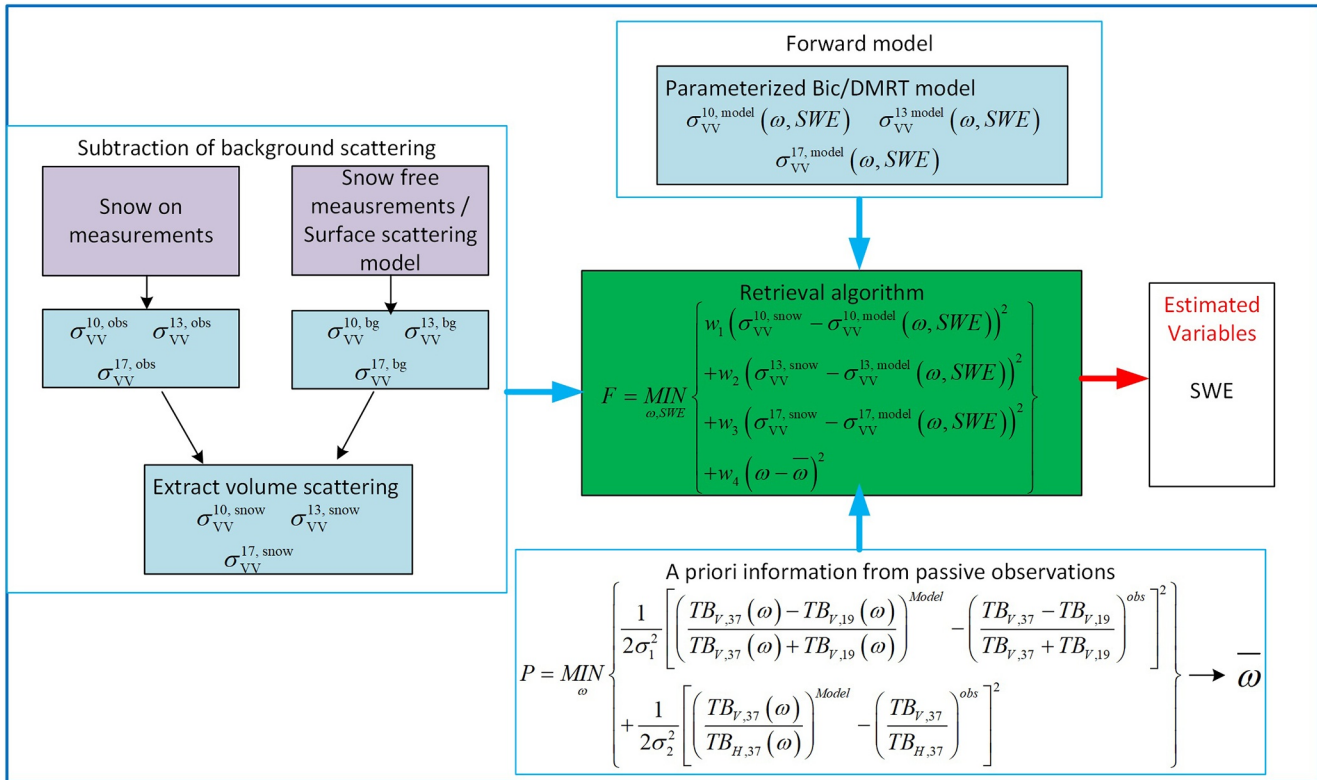
Figure 4. Illustration of a physical model based SWE retrieval algorithm using 10, 13, and 17 GHz radar channels aided with passive microwave observations at 19 and 37 GHz.

and TBs (Liang et al., 2008) of the snowpack. We simulate the scattering properties of the snowpack with a homogenous single-layer. The single-layer model is simple for both forward model and retrieval. If the effective grain size can be obtained accurately from the in situ measurement, the single-layer model can generate similar backscatter with the multi-layer model (King et al., 2018). The single-layer model is sensitive to snow grain size. The scattering contribution of smaller grains is less than that of larger grains (King et al., 2018). There are four input parameters for the DMRT-Bic model: snow density (ρ_{snow}), snow depth (d), and snow microstructure parameters (b and $\langle\zeta\rangle$) (Ding et al., 2010). The mean wave number $\langle\zeta\rangle$ with units of m^{-1} is inversely proportional to the mean grain size of snow. Parameter b is dimensionless and reflects the aggregation of snow particles (Xu et al., 2012). Then a parameterized model is derived by regression training with a backscatter LUT that makes the retrieval algorithm much more straightforward.

3.1.1. The LUTs for Active and Passive Observations

In Zhu et al. (2018), the active LUT of the snowpack has been generated at 10 and 17 GHz. The LUT covers the following snow parameters: ρ_{snow} varies from 91.7 to 412.7 kg/m^3 with a step of 45.9 kg/m^3, d starts from 0.1 to 1.5 m with a step of 0.1 m, parameter b varies between 0.6 and 1.6 with a step of 0.2 and $\langle\zeta\rangle$ varies from 5,000 to 15,000 m^{-1} with a step of 2,000 m^{-1} corresponding to snow grain size from 0.6 to 2 mm (W. Chang et al., 2016; Ding et al., 2010; Zhu et al., 2018). Based on the in situ measurements (Lemmetyinen et al., 2016), the snow properties during the NoSREx campaign are spanned by the LUT. This paper extends the active LUT by including 13 GHz. In addition, a new passive LUT of the snowpack with the same parameter ranges for 19 and 37 GHz passive observations was also generated. The simulations were performed at an elevation angle of 40° for all frequencies. Based on the ground measurements from the NoSREx, during the dry snow season, the average temperature of the snowpack and soil at 2 cm depth were 269 and 265 K, respectively. Both soil and snow temperature are treated as constant in simulations. The soil under dry snow conditions is treated as frozen. The relative permittivity of frozen soil is $\epsilon_g = 5 + i0.5$ according to the in situ measurements (Lemmetyinen et al., 2018).
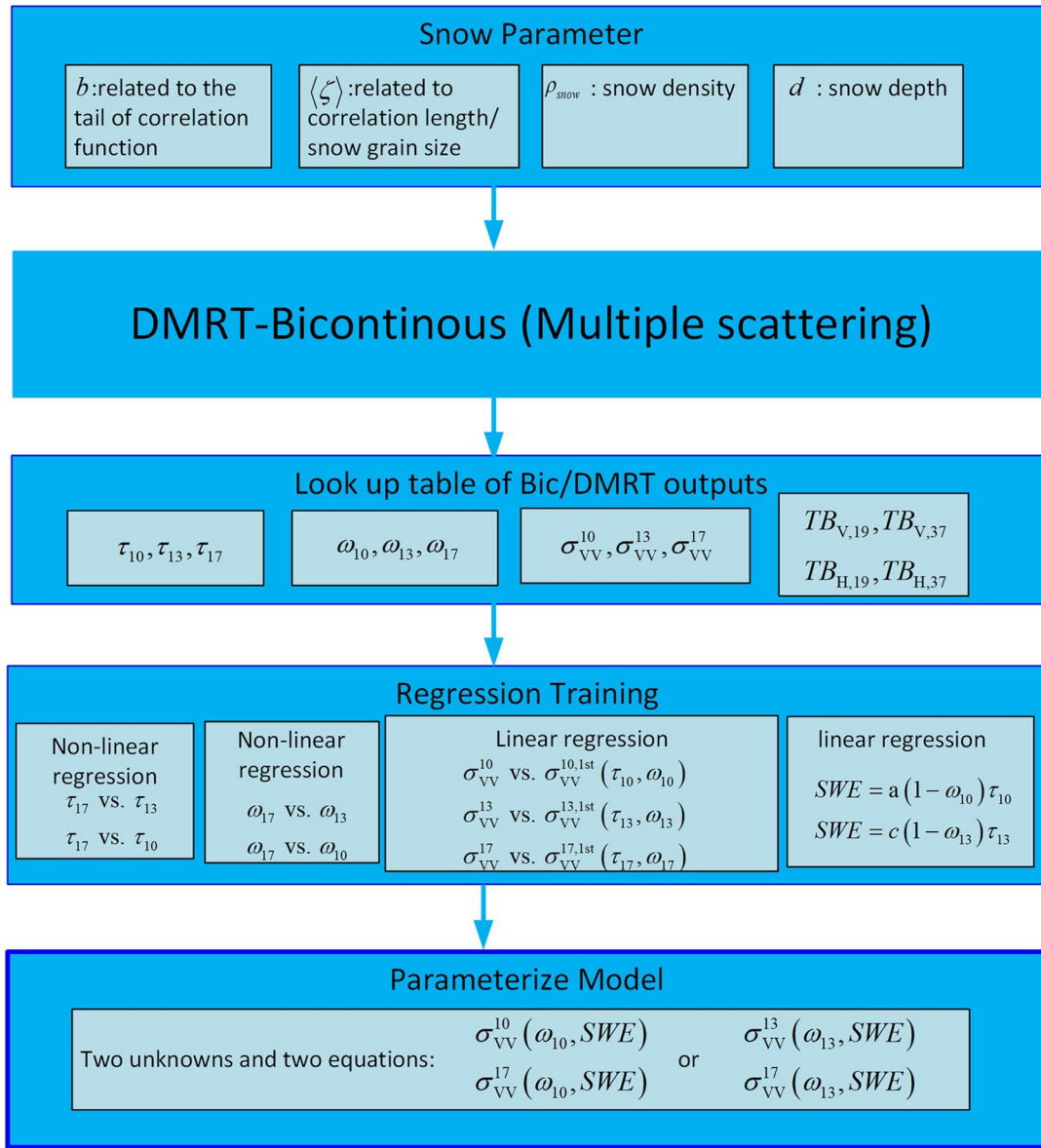
Figure 5. Flow diagram of the parameterized model of the bicontinuous dense media radiative transfer model from regression training. The superscript "1st" refers to first-order scattering of snow.

3.1.2. Regression Training: The Parameterized Model From the Active LUT for Snow Volume Scattering

The radiative transfer solution indicates that the first-order snow volume scattering is a function of ω and τ at the corresponding frequency, $\sigma_{VV}^{1st} = 0.75 \cos\theta_t \omega \left(1 - \exp\left(-2\tau / \cos\theta_t\right)\right)$ (Cui et al., 2016; Zhu et al., 2018). The transmitted angle in snow is θ_t. The first-order solution σ_{VV}^{1st} and multiple order solution σ_{VV} from the active LUT are strongly correlated. Therefore, snow volume scattering can be expressed by

$$\sigma_{VV}\left(dB\right) = A + B10\log_{10}\sigma_{VV}^{1st}\left(\omega, \tau\right) \tag{1}$$

Equation 1 is the parameterized model. In Zhu et al. (2018), the parameterized model for 10 and 17 GHz snow volume scattering was derived and is listed here in Table 1 (first and third rows). In this paper, we extend the parameterized model for snow volume scattering at 13 and 17 GHz. The procedure of regression training is illustrated in Figure 5 which follows Zhu et al. (2018). In the active LUT, 9 outputs have been tab-

Table 1
Summary of Coefficients and First-Order Scattering for Expressions of Snow Volume Scattering at 10, 13, and 17 GHz

Snow volume scattering	A	B	The first-order scattering σ_{VV}^{1st}
σ_{VV}^{10}	−2.81	0.96	$0.75\cos\theta_t\omega_{10}\left[1-\exp\left(\dfrac{-2\mathrm{SWE}}{a\left(1-\omega_{10}\right)\cos\theta_t}\right)\right]$
			$a=9745$ (Zhu et al., 2018)
σ_{VV}^{13}	−1.6	1.00	$0.75\cos\theta_t\omega_{13}\left[1-\exp\left(\dfrac{-2\mathrm{SWE}}{c\left(1-\omega_{13}\right)\cos\theta_t}\right)\right]$
			$c=4683$
σ_{VV}^{17} vs σ_{VV}^{10}	0.05	1.12	$0.75\cos\theta_t\left(\dfrac{\omega_{10}}{0.66\omega_{10}+0.37}\right)\left[1-\exp\left(-\dfrac{2}{\cos\theta_t}\left(5.37\left(\dfrac{\mathrm{SWE}}{a\left(1-\omega_{10}\right)}\right)^{0.97}\right)\right)\right]$
			$a=9745$ (Zhu et al., 2018)
σ_{VV}^{17} vs σ_{VV}^{13}	0.05	1.12	$0.75\cos\theta_t\left(\dfrac{\omega_{13}}{0.32\omega_{13}+0.69}\right)\left[1-\exp\left(-\dfrac{2}{\cos\theta_t}\left(1.87\left(\dfrac{\mathrm{SWE}}{c\left(1-\omega_{13}\right)}\right)^{0.97}\right)\right)\right]$
			$c=4683$

Note. θ_t is the transmitted angle within the snowpack.

ulated: the scattering albedo $\omega_{10}, \omega_{13}, \omega_{17}$, the optical thicknesses $\tau_{10}, \tau_{13}, \tau_{17}$, and VV snow volume scattering $\sigma_{VV}^{10}, \sigma_{VV}^{13}, \sigma_{VV}^{17}$ at 10, 13, and 17 GHz. Regression training is conducted for ω_{17} versus ω_{13} and τ_{17} versus τ_{13}. The regression formulas are

$$
\begin{aligned}
\omega_{17} &= \frac{\omega_{13}}{0.32\omega_{13}+0.69}\\
\tau_{17} &= 1.87\left(\tau_{13}\right)^{0.97}
\end{aligned}
\tag{2}
$$

In Figures 6a and 6b, the regression curves represent the simulations of LUT well. For ω_{17} and ω_{13}, the coefficient of determination is 0.99. For τ_{17} and τ_{13}, the coefficient of determination is 0.99. In addition, a similar relationship between $\sigma_{VV}^{13,1st}$ and σ_{VV}^{13} was derived, listed in Table 1 second row. The RMSE in regression is 0.96 dB and the coefficient of determination is ∼0.94 for the 13 GHz channel, as shown in Figure 6c. With the relationship that the absorption loss $\tau_a = (1-\omega)\tau$ is proportional to SWE (Cui et al., 2016; Zhu et al., 2018), the regression formula between the absorption and SWE at 13 GHz based on LUT is

$$
\mathrm{SWE} = c\left(1-\omega_{13}\right)\tau_{13}
\tag{3}
$$

where $c = 4{,}683$. As illustrated in Figure 6d, Equation 3 shows a strong relationship with an RMSE of ∼16 mm and a coefficient of determination of ∼0.96. Thus, the snow volume scattering of 13 and 17 GHz as a function of SWE and ω_{13} is obtained and listed Table 1 (second and fourth rows). For either pair of frequencies (10&17 GHz or 13&17 GHz), σ_{VV} is only dependent upon two unknowns which leads to a retrieval that has two observations and two unknowns. Such a parameterized model is simpler and more efficient for retrieval than a fully physics-based model. With such characterization of the snowpack, ω and SWE are the only two parameters retrieved in the retrieval algorithm.

3.2. Determination of Background Scattering

In this paper, the Oh model will be applied to retrieve the soil permittivity and roughness with radar observations at 10 GHz (Oh et al., 1992) just before snowfall or under thin snow conditions. With the retrieved
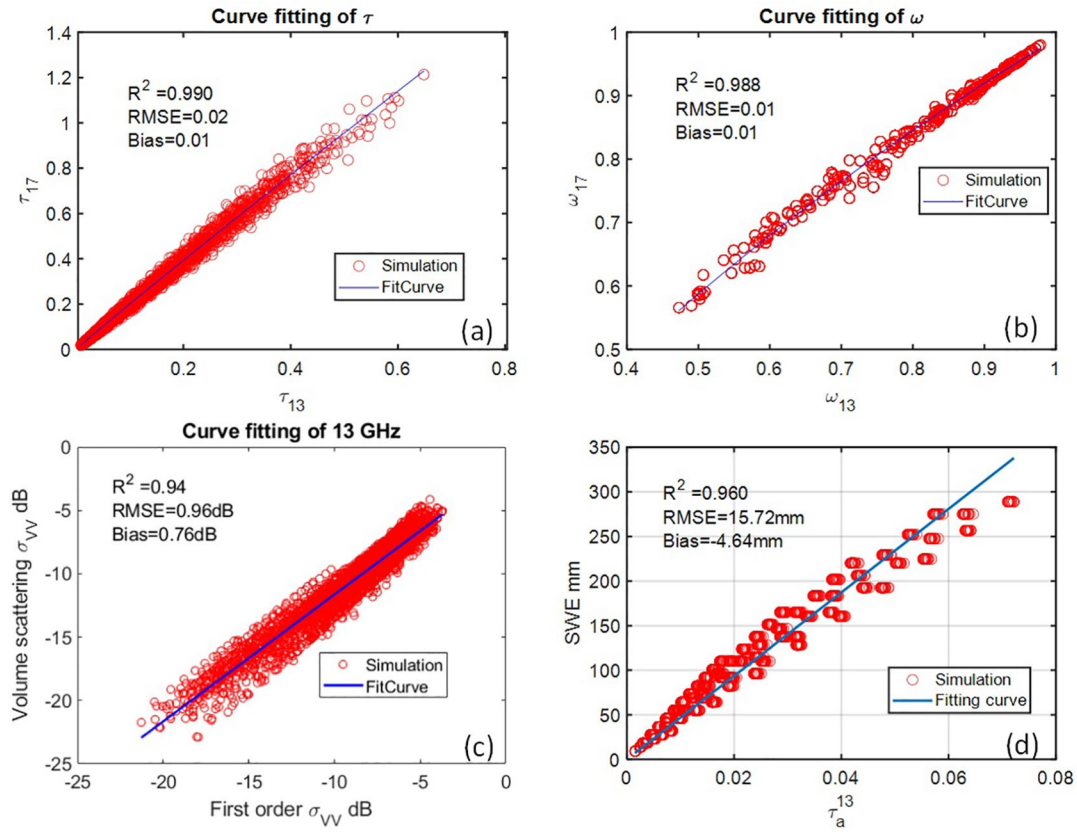
Figure 6. Summary of regression trainings and their accuracy. Comparison of parameters between simulation and regression results: (a) optical thickness, (b) scattering albedo, (c) multiple scattering and first-order regression at 13 GHz, and (d) SWE as a function of the absorption loss at 13 GHz, τ_a^{13}. The circles are simulation results from the look-up table (LUT) and the lines are the regression curves.

roughness, the background scattering at 10, 13, and 17 GHz are calculated using the Oh model. The total backscatter (radar observations) consist of volume scattering from snow and background scattering from the snow/ground interface, which is described by the expression as (Cui et al., 2016; Xu et al., 2012):

$$\sigma_{\mathrm{VV}}^{\mathrm{obs}} = \sigma_{\mathrm{VV}}^{\mathrm{bg}} \exp\left(-2\tau / \cos\theta_t\right) + \sigma_{\mathrm{VV}}^{\mathrm{snow}} \tag{4}$$

where $\sigma_{\mathrm{VV}}^{\mathrm{snow}}$ is the contribution from volume scattering of snowpack and $\sigma_{\mathrm{VV}}^{\mathrm{bg}}$ is the background scattering component attenuated by snowpack with a factor of $\exp\left(-2\tau / \cos\theta_t\right)$. In this paper, the transmitted angle θ_t is calculated by assuming a constant snow permittivity of 1.45. Based on Zhu et al. (2018) and Equation 3, $\tau_{10} = \mathrm{SWE} / a\left(1 - \omega_{10}\right)$ and $\tau_{13} = \mathrm{SWE} / c\left(1 - \omega_{13}\right)$ in the retrieval algorithm. The volume scattering component is the component sensitive to snow information such as SWE. The background scattering component reduces the sensitivity of the total backscatter to SWE. The effects of background scattering decrease with increasing SWE or frequency. With Equation 4, the volume scattering component can be extracted from the total backscatter.

Background scattering at a given frequency is determined by two key parameters of the underlying ground (assuming the ground is bare soil): soil permittivity and roughness (rms height) (Oh et al., 1992). We make a simplifying assumption that the roughness of the soil surface remains constant from the time of the snow-free observation and the time of the SWE retrieval, and that this is the case for all soil conditions. The soil permittivity depends on the freeze/thaw state and soil moisture. It is possible that soil is unfrozen before snow accumulation. If independent freeze/thaw state information is not available, then an alternative such as using time-series radar observations is needed to retrieve both roughness and soil permittivity. Fortunately, in the the NoSREx campaign, the soil was frozen or near-frozen after November, as shown by Figure 2.
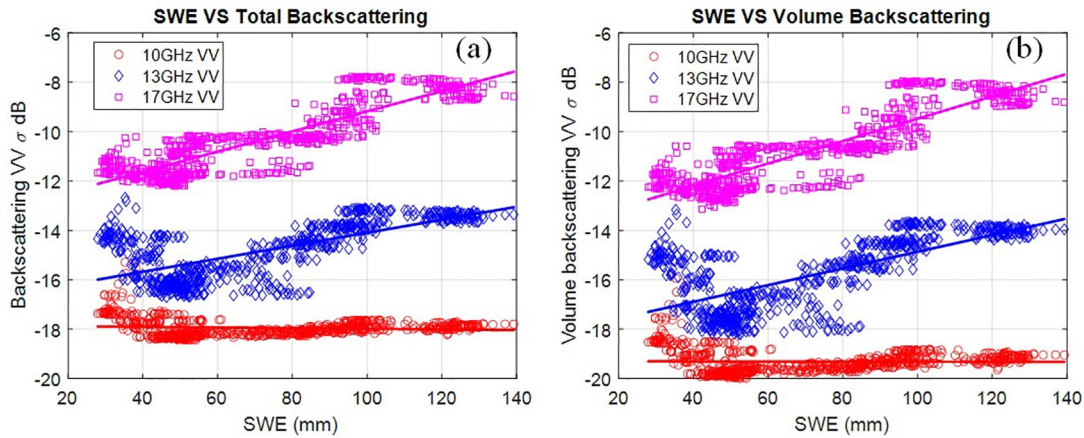
Figure 7. Vertically co-polarized backscatter as a function of SWE from the NoSREx 2010–2011 data: (a, left) total backscatter versus SWE and (b, right) volume scattering component of backscatter versus SWE.

Thus, the permittivity of frozen soil is constant through the winter, and we assume a value of $\epsilon_g = 5 + i0.5$. With this soil permittivity, we select radar observations around November 10, 2010 (−17.4 dB at 10 GHz) for retrieval of soil roughness, though there is snow cover with a depth of 18 cm. For 18 cm snow, total backscatter at 10 GHz is dominated by the background scattering. With the Oh model, the retrieved rms surface roughness is 2 mm. With this rms height and soil permittivity, the background scattering at 10, 13, and 17 GHz are calculated using the Oh model. The calculated background scattering at the three frequencies are used in the retrieval for all seasons. Note that such an approach assumes that soil conditions are constant during the period of applicability of this algorithm (the dry snow season).

In Figure 7, the total backscatter (a) from the NoSREx 2010–2011 is compared with the volume scattering (b) at 10, 13, and 17 GHz. The volume scattering is obtained by subtracting the background scattering from radar observations with Equation 4. We find τ and $\cos\theta_t$ using in situ measurements and the DMRT-Bic LUT. The comparison reveals that the volume scattering components for SWE below 100 mm are 1.6 dB below the total backscatter at 10 GHz, 1 dB at 13 GHz, and 0.5 dB at 17 GHz. This means that the background scattering is 45%, 25%, and 12% of the volume scattering of snow, respectively. Therefore, the effects of the background are weaker at 13 and 17 GHz.

3.3. The Combined Active and Passive Retrieval Algorithms

Passive microwave observations (TBs) of snow are also based on volume scattering by the snowpack. The volume scattering increases with the fourth power of frequency and the third power of the grain size of snow, if Rayleigh scattering is assumed (Tsang et al., 2004; Xu et al., 2012). Therefore, high-frequency passive observations are highly sensitive to snow microstructure, which we utilize to estimate an a priori ω.

As illustrated in Figure 4, the passive observations are compared with the passive LUT to determine ω. The passive observations of the snowpack depend on the physical temperatures of the snow and the ground, SWE, and the scattering albedo ω. For example, at 37 GHz and V-polarization

$$\text{TB}_{V,37} = a_{V,37}\left(\text{SD}, \omega_{37}\right)\text{T}_{\text{snow}} + \exp\left(-\tau_{37} / \cos\theta_t\right)e_{V,g}T_g \tag{5}$$

where $a_{V,37}$ is the absorption of snowpack, which depends on snow depth (SD) and scattering albedo ω_{37} at 37 GHz. The physical temperature of snow and ground are T_{snow} and T_g, respectively. The ground emissivity is $e_{V,g}$. Because of strong volume scattering at 37 GHz, the optical thickness τ_{37} at 37 GHz is large. Thus, we can ignore the effect of the ground at 37 GHz. With the ratio of V- and H-polarization TBs at 37 GHz $\text{TB}_{V,37}/\text{TB}_{H,37}$, the physical temperature cancels out. Therefore, with passive observations at 37 GHz, SD is also needed to determine the scattering albedo ω_{37}. In order to avoid using in situ snow depth, we apply the passive observa-
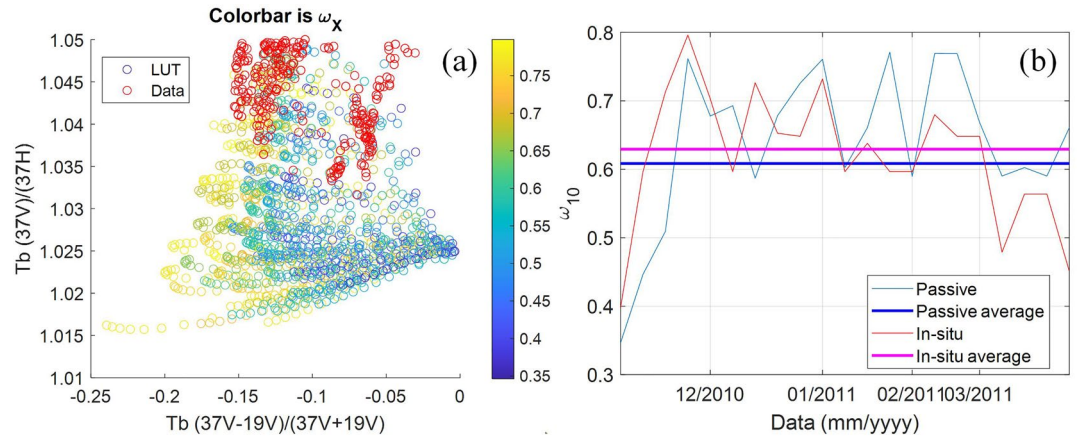
Figure 8. (a, left) Comparison of the passive observations of 2010–2011 (red circles) and passive LUT (other color circles) in terms of $TB_{V,37} - TB_{V,19} / TB_{V,37} + TB_{V,19}$ and $TB_{V,37} / TB_{H,37}$. The color bar is ω_{10}. (b, right) Comparison of retrieved ω from in situ measurements and passive obervations.

tions to retrieve snow depth (Markus & Cavalieri, 1998), $SD = d_1 + d_2 \left(TB_{V,37} - TB_{V,19} / TB_{V,37} + TB_{V,19} \right)$, where d_1 and d_2 are coefficients derived from in situ measurements and passive observations. This indicates that $TB_{V,37} - TB_{V,19} / TB_{V,37} + TB_{V,19}$ is proportional to SD, which can help in our algorithm to determine the scattering albedo. Therefore, a simple cost function is established to find the best match in passive LUT with the passive observation.

$$
P = \operatorname*{MIN}_{\omega} \left\{ \frac{\left[\left(\frac{TB_{V,37}(\omega) - TB_{V,19}(\omega)}{TB_{V,37}(\omega) + TB_{V,19}(\omega)} \right)^{\text{Model}} - \left(\frac{TB_{V,37} - TB_{V,19}}{TB_{V,37} + TB_{V,19}} \right)^{\text{obs}} \right]^2}{2 p_1^2} \right.
$$

$$
\left. + \frac{\left[\left(\frac{TB_{V,37}(\omega)}{TB_{H,37}(\omega)} \right)^{\text{Model}} - \left(\frac{TB_{V,37}}{TB_{H,37}} \right)^{\text{obs}} \right]^2}{2 p_2^2} \right\}
\tag{6}
$$

where V and H mean polarizations. The standard deviation p_1 and p_2 are obtained from

$$
\begin{aligned}
p_1 &= \operatorname{std} \left\{ \operatorname{MIN} \left| \left(\frac{TB_{V,37} - TB_{V,19}}{TB_{V,37} + TB_{V,19}} \right)^{\text{Model}} - \left(\frac{TB_{V,37} - TB_{V,19}}{TB_{V,37} + TB_{V,19}} \right)^{\text{obs}} \right| \right\} \\
p_2 &= \operatorname{std} \left\{ \operatorname{MIN} \left| \left(\frac{TB_{V,37}}{TB_{H,37}} \right)^{\text{Model}} - \left(\frac{TB_{V,37}}{TB_{H,37}} \right)^{\text{obs}} \right| \right\}
\end{aligned}
\tag{7}
$$

We compare the model predictions with the each set of observations to find the minimum value. Considering all sets of observations, p_1 and p_2 are calculated by taking the standard deviation. With the NoSREx 2010–2011 dataset, we get $p_1 = 5.99 \times 10^{-5}$ and $p_2 = 0.0076$. In this paper, for all seasons, we use same values of p_1 and p_2.

We use Equation 6 to derive ω from passive observations. The first term in Equation 6 includes information on snow depth. Since the higher frequency is more sensitive to the scattering albedo, we use the TB polarization ratio at 37 GHz in the second term. As shown in Figure 5, there are 13 tabulated outputs from the DMRT-Bic model: the scattering albedo $\omega_{10}, \omega_{13}, \omega_{17}$, the optical thicknesses $\tau_{10}, \tau_{13}, \tau_{17}$, and VV snow volume

scattering $\sigma_{VV}^{10}, \sigma_{VV}^{13}, \sigma_{VV}^{17}$, and TB of 19 and 37 GHz $TB_{V,19}, TB_{H,19}, TB_{V,37}, TB_{H,37}$. These 13 outputs are correlated and corresponding to the same simulated snowpack. After finding the best match TB with Equation 6 for each set of observations, the associated ω_{10} and ω_{13} are obtained simultaneously.

Note that, by using Equation 6, there are several assumptions included. The passive LUT is generated by assuming constant temperatures for both snow and ground. The paper also assumes that the effect of ground is negilible for TB at 37 GHz. SD is retrieved by using passive observations, which includes errors from the retrieval. Such a retrieval approach is also affected by physical temperatures and ground conditions. These facts can cause uncertainties for the estimation of scattering albedo. In this paper, we focus on the preliminary examination of the method and ignore these effects. In the future, we will quantitatively study the uncertainties of these assumptions and consider using ancillary data of temperatures, ground conditions, and SD to improve the accuracy of the scattering albedo estimation.

Multiple passive observations in time series are acquired to help improve the estimation. A priori $\bar{\omega}$ is the average of all the retrieved ω. In this paper, for each season, we use time series passive observations during the dry snow season to obtain a single a priori $\bar{\omega}$ and apply it to the retrieval for the whole season. As an example, we derive a priori $\bar{\omega}_{10}$ for the 2010–2011 winter season. In Figure 8a, we plot the passive observations in terms of $TB_{V,37} - TB_{V,19} / TB_{V,37} + TB_{V,19}$ and $TB_{V,37} / TB_{H,37}$ against the passive LUT. Generally, $TB_{V,37} - TB_{V,19} / TB_{V,37} + TB_{V,19}$ decreses with the increase of ω_{10}. Most of passive observations are located around the region of $\omega_{10} = 0.6$. By using snowpit measurements and microwave observations simultaneously measured when snowpit was being excavated, we can estimate the scattering albedo. The detailed procedure is as follows: First, we follow Zhu et al. (2018) to find the associated ω_{10} for each pair of radar observations by using in situ measurements. The volume scattering components of the total radar observations are obtained by excluding background scattering (determined in Section 3.2). Next, the co-located SWE and snow density measurements are taken as known parameters. With these two parameters, we search for the best ω_{10} to match with the volume scattering components of the total radar observations using the parameterized model. The best match ω_{10} is the associated ω for the corresponding pair of radar observations. A priori $\bar{\omega}_{10}$ is the average of associated ω_{10} of all radar observations, $\bar{\omega}_{10} = 0.63$. The retrieved ω_{10} and $\bar{\omega}_{10}$ from the in situ measurements are taken as a benchmark and illustrated in Figure 8b. Next, we apply the passive observations collected at the same time as snowpit measurements to determine ω_{10} with Equation 6, where no ground measurements are required. The determined $\bar{\omega}_{10}$ is the average of all the retrieved ω_{10} from passive observations, $\bar{\omega}_{10} = 0.61$. Comparing the retrieved ω_{10} from in situ measurements and passive observations, the RMSE is about 0.1 and the correlation is 0.525. These two results are moderately correlated. In the early season, the retrieved ω_{10} from passive observations tend to be similar with that of in situ measurements. While ω_{10} from passive observations is overestimated in the late season. Fortunately, both of the retrieved ω_{10} have almost same average values. Since it is hard to get the retrieved ω_{10} from passive observations that accurately at the local time period, we need to use the average to reduce estimation errors. In Section 6, we have tested this for multiple years of observations, and the approach provides sufficient fidelity for our purposes.

With this *a priori* $\bar{\omega}$ from passive observations, the active retrieval algorithm is applied. The cost function is guided by *a priori* $\bar{\omega}$ to avoid getting trapped in a local minimum. Through this minimization, the algorithm retrieves both ω and SWE. The active algorithm refines the estimation of ω, which enhances the sensitivity of backscatter to SWE.

For the SWE retrieval, a least-square cost function constrained by *a priori* $\bar{\omega}$ is applied to fit the parameterized model results into radar observations (Cui et al., 2016; Zhu et al., 2018). Although using three frequency radar observations provides more information, it also involves more uncertainties. In the cost function, only two-frequency radar observations which give the best sensitivity to SWE are selected. The cost function is given as:

$$F = \min_{\omega, \text{SWE}} \left\{ \frac{\left(\sigma_{VV}^{1,\text{snow}} - \sigma_{VV}^{1,\text{model}}(\omega, \text{SWE}) \right)^2}{2s_1^2} + \frac{\left(\sigma_{VV}^{2,\text{snow}} - \sigma_{VV}^{2,\text{model}}(\omega, \text{SWE}) \right)^2}{2s_2^2} + \frac{(\omega - \bar{\omega})^2}{2s_\omega^2} \right\} \qquad (8)$$

Table 2
A Priori Scattering Albedo Determined From In Situ Measurements and Passive Observations

Method	Scattering albedo	2009–2010	2010–2011	2012–2013
In situ measurements	$\bar{\omega}_{10}$	0.58	0.63	0.44
	$\bar{\omega}_{13}$	0.64	0.65	0.51
Passive observations	$\bar{\omega}_{10}$	0.59	0.61	0.48
	$\bar{\omega}_{13}$	0.67	0.65	0.55

where $\sigma_{VV}^{1,\text{snow}}, \sigma_{VV}^{2,\text{snow}}$ are radar observations of VV-polarization at dual frequencies excluding background scattering from the snow/ground interface (which is determined in Section 3.2). $\sigma_{VV}^{1,\text{model}}, \sigma_{VV}^{2,\text{model}}$ are the backscatter predictions from the parameterized model. The reason that VV observations are used in the retrieval rather than HH (horizontal co-polarization) is that HH backscatter will have a stronger background scattering contribution than in the case of VV. This is apparent since the Fresnel reflection coefficients of the snow/soil interface at H-polarization are larger than at V-polarization. $\bar{\omega}$ is an *a priori* value for the scattering albedo determined from passive observations. s_1^2, s_2^2 are the expected error standard deviation of the radar measurements, and s_ω^2 act as the variance of the *a priori* constraint. Each term is normalized by assuming a Gaussian distribution. According to Cui et al. (2016) and Zhu et al. (2018), s_1 and s_2 are assumed to be 0.5, which are based on the error standard deviation of radar measurements. We also set s_ω to be 0.1.

4. Results

In this section, the combined active and passive retrieval algorithm is validated against the NoSREx dataset. We test the retrieval algorithm for three sets of frequency combinations:

1. SWE Retrieval with 10 and 17 GHz channels and $\bar{\omega}_{10}$ as *a priori* information.
2. SWE Retrieval with 13 and 17 GHz channels and $\bar{\omega}_{13}$ as *a priori* information.
3. First, retrieve with 13 and 17 GHz channels using $\bar{\omega}_{13}$. If the retrieved SWE is large than 80 mm, do another retrieval with 10 and 17 GHz channels using $\bar{\omega}_{10}$.

The threshold of 80 mm is chosen since it is near the median value of SWE measurements. The idea is to create an adaptive way to combine three frequencies. Since the backscatter of 13 and 17 GHz is less affected by the background scattering, retrieval based on 13 and 17 GHz channels may be better for thin snow.

In addition, the paper also compared the combined active and passive algorithm with the active-only algorithm. In the active-only algorithm, *a priori* $\bar{\omega}$ is determined with the in situ measurements and radar observations. As introduced in Section 3.3, we calculate a priori $\bar{\omega}$ at 10 and 13 GHz following Zhu et al. (2018). In this paper, *a priori* $\bar{\omega}$ and the performance of the active-only algorithm are regarded as benchmarks since ground measurements are applied. For the combined active and passive algorithm, only passive observations are applied to determine $\bar{\omega}$ with Equation 6. In this section, we select the passive observations which correspond to the simultaneous TB scenes when the snowpit was being excavated. In Table 2, we list *a priori* $\bar{\omega}_{10}$ and $\bar{\omega}_{13}$ determined from these two methods. Generally, results of these two methods agree well. In retrieval, both the active-only and combined method use a single *a priori* $\bar{\omega}$ for the whole season.

SWE retrieval performance for the active-only algorithm is shown in Table 3, while retrieval performance of the combined active-passive algorithm is listed in Table 4. Both tables list the achieved RMSE, correlation, and bias of SWE retrieval to facilitate intercomparison. The retrieval results of 2010–2011 achieved the best RMSE (<21 mm) and correlation (>0.85) while the results of 2012–2013 were the worst. Comparing the performance among the three sets of frequency combinations, we found the retrieval based on 13 & 17 GHz for 2009–2011 usually had the best RMSE and correlation (except for the combined active-passive method for 2009–2010 in which the $\bar{\omega}_{13}$ is overestimated). In contrast, for 2012–2013, the retrieval of 13 & 17 GHz gives the worst RMSE and correlation. Using all three frequencies does not result in better performance than the dual-frequency retrieval—at least for the snow conditions encountered at NoSREX. This may be because the snowpack was not thick enough

Table 3
Performance of Active-Only Snow Water Equivalent (SWE) Retrieval Using NoSREx Campaign Data

Year	Radar channel	Correlation coefficient	RMSE (mm)	Bias (mm)
2009–2010	10 & 17 GHz	0.693	26.30	14.50
	13 & 17 GHz	0.698	23.21	5.13
	Combining 10, 13, 17 GHz	0.685	27.70	15.37
2010–2011	10 & 17 GHz	0.860	17.05	−0.70
	13 & 17 GHz	0.872	15.94	−1.01
	Combining 10, 13, 17 GHz	0.859	17.19	0.74
2012–2013	10 & 17 GHz	0.585	31.71	1.54
	13 & 17 GHz	0.377	35.71	−1.94
	Combining 10, 13, 17 GHz	0.585	31.71	1.59

Table 4
Performance of Combined Active-Passive SWE Retrieval Using NoSREx Campaign Data

Year	Radar channel	Correlation coefficient	RMSE (mm)	Bias (mm)
2009–2010	10 & 17 GHz	0.691	22.03	2.81
	13 & 17 GHz	0.698	24.86	−9.19
	Combining 10, 13, 17 GHz	0.684	24.46	8.44
2010–2011	10 & 17 GHz	0.860	19.73	5.24
	13 & 17 GHz	0.875	15.99	0.15
	Combining 10, 13, 17 GHz	0.857	20.08	3.07
2012–2013	10 & 17 GHz	0.587	36.22	−20.30
	13 & 17 GHz	0.387	39.42	−19.34
	Combining 10, 13, 17 GHz	0.585	36.14	−20.24

to result in differentiations among the three frequencies that were large compared to the corresponding uncertainties at those frequencies.

Comparing the combined active-passive and the active-only algorithms, the combined algorithm achieves similar performance, which reveals that passive observations do help to provide an acceptable *a priori* scattering albedo. As an example, SWE retrieval performance for both algorithms for 2010–2011 are shown in Figure 9. In Figure 10, the SWE retrieval performance using the combined active-passive algorithm with 10 & 17 GHz and with 13 & 17 GHz are compared with measured SWE for all three winters.

For the SWE retrieval of NoSREx 2010–2011, overall, retrieved SWE is in reasonable agreement with measured SWE. However, there are some inconsistencies. The retrieved SWE overestimates the SWE and gradually decreases in the early season (Figures 10b and 10e). This is because the backscatter of 13 and 17 GHz was decreasing in the early season (see Section 2 for additional explanation). We also find retrieved SWE based on 10 and 17 GHz (Figures 9a and 9d or Figure 10b) does not change for measured SWE between 60 and 100 mm. Some inconsistent SWE were found caused by errors from automated measurements as mentioned in Section 2. Another potential reason is that although the SWE increased from 60 to 100 mm, 10 and 17 GHz backscatter hardly increased during January 1 to February 1 of 2011 (Figure 2b). However, the 13 GHz backscatter increased with SWE leading to better performance with 13 and 17 GHz (Figures 9b and 9e or Figure 10e). From January 1 to February 1, as shown in Figures 3c and 3d, the snow accumulation was mostly from the top layer. The grain size of top layer decreased while the bottom layer grain size increased. For 17 GHz, these two effects canceled each other leading to constant backscatter. However, because of its longer wavelength, the backscatter at 13 GHz was affected more by the change of the bottom layer. For measured SWE above 100 mm, there might be measurement errors in the middle of February where the SWE fluctuates. The 10 and 17 GHz retrieval (Figure 10b) overestimates SWE for measured SWE above 100 mm while the 13 and 17 GHz retrieval (Figure 10e) provides reasonable results. The early season inconsistency and the inconsistency in the February 2011 retrieval using 10 and 17 GHz demonstrates the possibility that an increase of SWE does not lead to an increase of backscatter. The retrieval algorithm currently does not address this problem well. It implies a limitation of the algorithm due to its use of a single-layer model with a single a priori scattering albedo and insufficient degrees of freedom to adequately represent the actual impact of stratigraphy.

The retrieval for 2009–2010 (Figures 10a and 10d) also achieves reasonable performance in general. However, it also has similar inconsistencies in the early season and February 2010 as those for 2010–2011, as shown by Figure 2a. These inconsistencies are more distinct and affect a longer period, which makes the retrieval performance of 2009–2010 worse than that of 2010–2011. In addition, the $\bar{\omega}_{13}$ from passive observations is overestimated which leads to underestimation of SWE beginning in the middle of February 2010 for the 13 and 17 GHz retrieval.

The retrieval for 2012–2013 (Figures 10c and 10f) gives the worst performance. In general, the retrieved SWE is underestimated compared with measured SWE. One reason is that both $\bar{\omega}_{10}$ and $\bar{\omega}_{13}$ from passive observations are overestimated. The other more important reason is that, similar to 2009–2010 and 2010–2011, the backscatter of 13 and 17 GHz decreased from December 1, 2012 to January 1, 2013 and subsequently remained stable until the middle of February 2013 (Figure 2d), which causes the most distinct inconsistencies in retrieval among three seasons.

5. Discussion

In the retrieval, uncertainty of the magnitude of background scattering directly impacts SWE retrieval accuracy. When radar observations are not available just before the snow accumulation period or soil conditions change during the dry snow season, we cannot obtain an exact magnitude of background scattering contri-
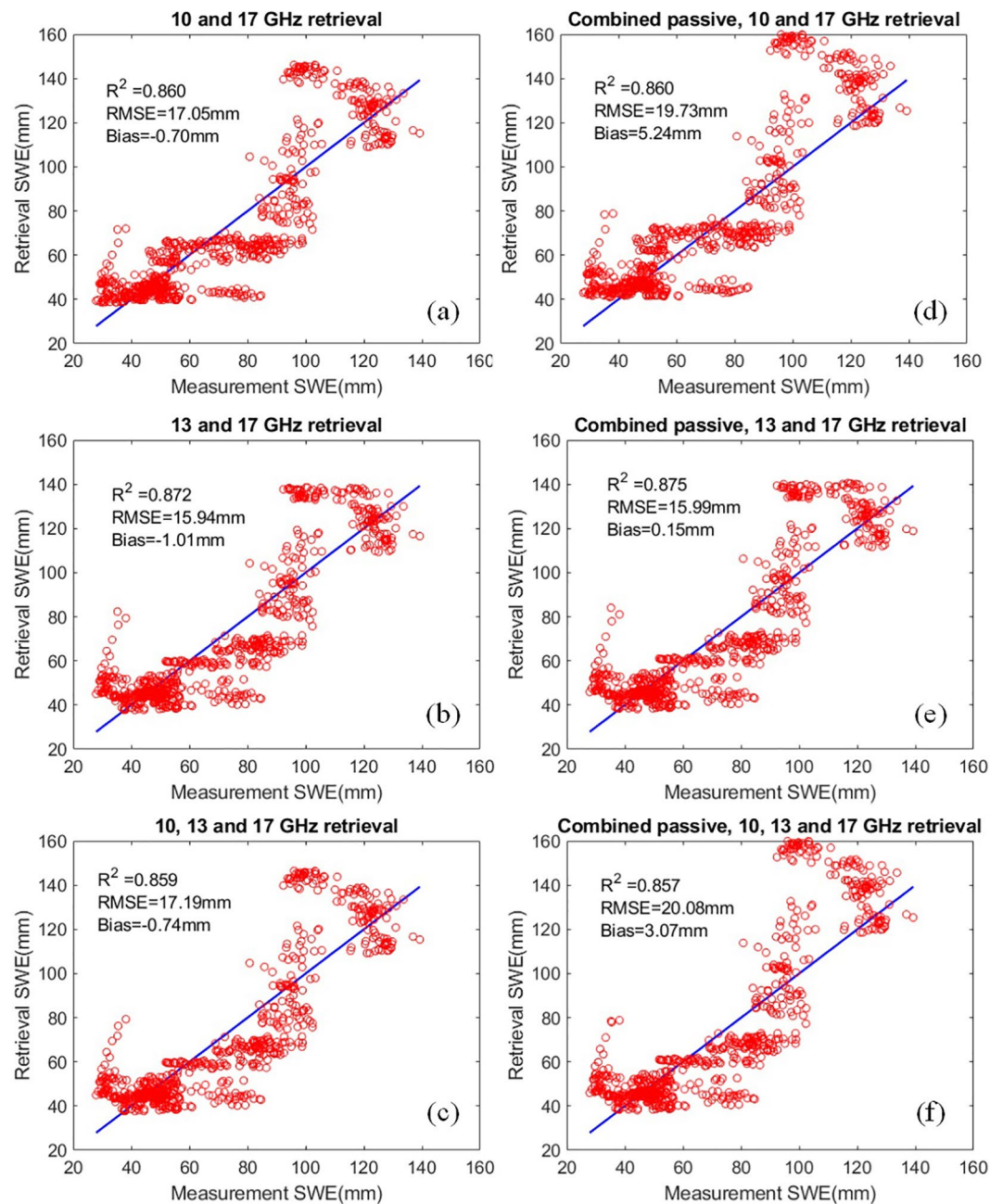
Figure 9. Comparison of SWE retrieved with SWE measured for the NoSREx campaign 2010–2011 data. (Left) retrieval based on the active-only algorithm using (a, top) 10 & 17 GHz, (b, middle) 13 & 17 GHz and (c, bottom) using all three frequencies. (Right) retrieval based on the combined active-passive algorithm using (d, top) 10 & 17 GHz, (e, middle) 13 & 17 GHz and (f, bottom) using all three frequencies.

bution. To better understand the impact of this uncertainty, the SWE retrieval of the active-only algorithm is tested based on the total backscatter without subtracting the background scattering (Figure 11). Figures 11a shows that the retrieval results with 10 and 17 GHz backscatter overestimate the SWE (the RMSE increases by 8 mm compared with Figure 9a) because the total backscatter is assumed to be entirely from snow volume scattering. The retrieval results based on 13 and 17 GHz backscatter as shown in Figures 11b show the retrieval using 13 and 17 GHz backscatter which still overestimates for SWE below 60 mm but provides better retrieval results than that of 10 and 17 GHz for SWE above 60 mm (the RMSE increases by 3 mm
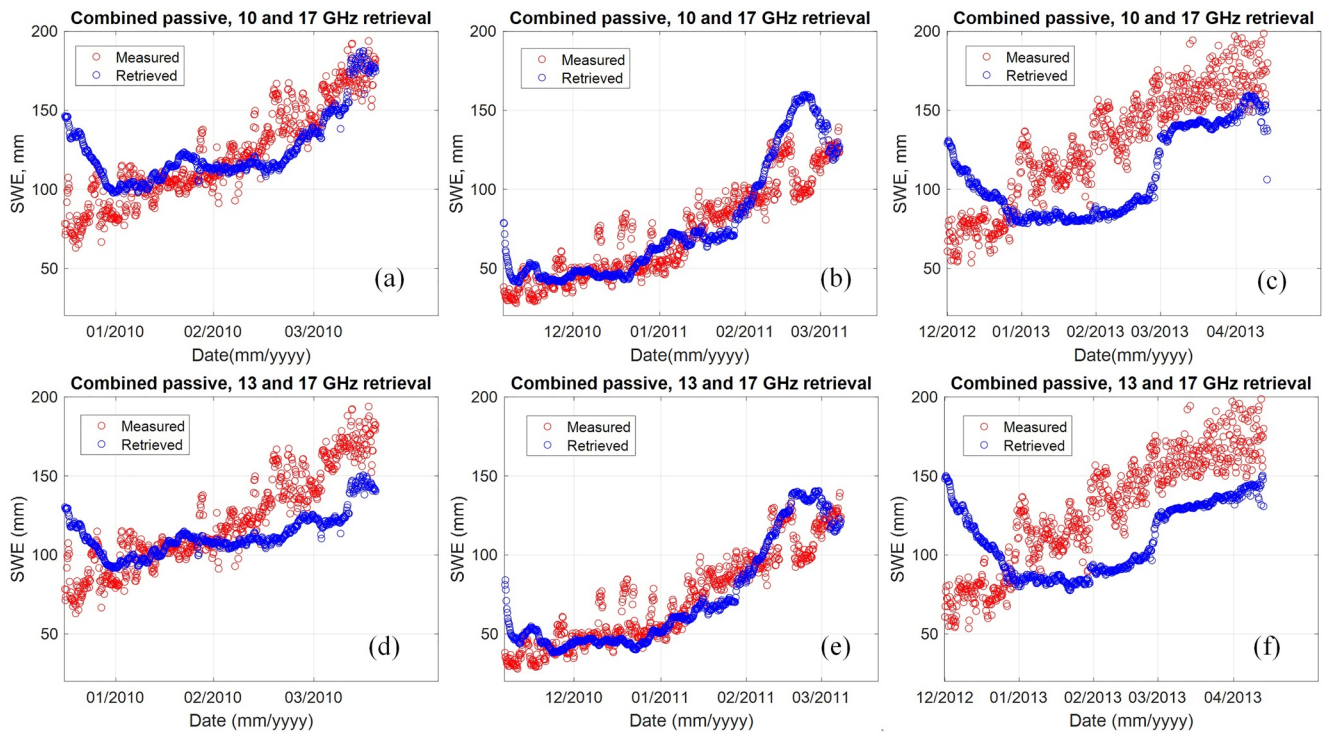
Figure 10. Measured SWE compared with SWE retrieved using the combined active-passive method for the NoSREx campaign. The retrievals in the top figures are based on 10 and 17 GHz: (a, left) 2009–2010, (b, middle) 2010–2011, and (c, right) 2012–2013. The retrievals in the bottom figures are based on 13 and 17 GHz: (d, left) 2009–2010, (e, middle) 2010–2011, and (f, right) 2012–2013.

compared with Figure 9b). Therefore, for the NoSREx site, using both Ku frequencies limits the background effects and improves SWE retrieval.

We examined how TB measurement uncertainty would affect the estimation of *a priori* information. Figure 12 illustrates the TB for V and H polarization at 19 and 37 GHz as a function of scattering albedo at 10 and 13 GHz from the DMRT-Bic LUT. TB of both polarizations at 19 GHz are not sensitive to scattering albedo until it is larger than 0.75 in both Figures 12a and 12b. Thus, using the 19 GHz TB channel to estimate scattering albedo of snow can be affected by measurement errors. However, TB at 37 GHz for both polarizations show good sensitivity to scattering albedo. The change of scattering albedo with $\Delta\omega = 0.1$ can have
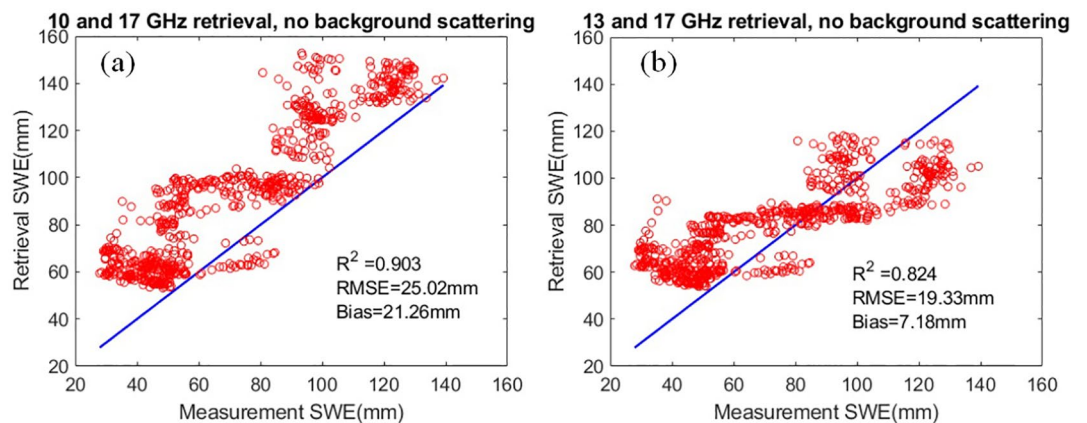

Figure 11. SWE retrieved results with of the active-only algorithm without background scattering subtraction for the NoSREx 2010–2011. (a, left) using 10 and 17 GHz retrieval and (b, right) using 13 and 17 GHz retrieval.
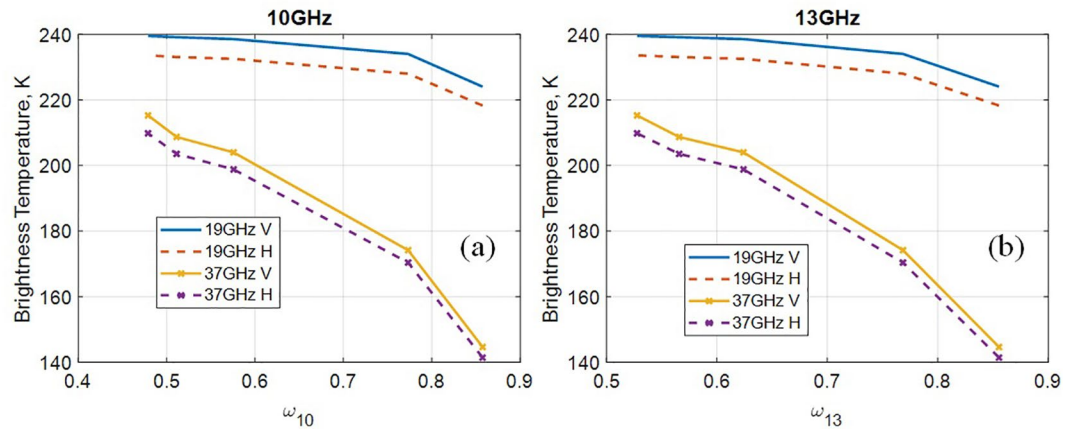
Figure 12. Sensitivity of TB at 19 and 37 GHz to scattering albedo at (a, left) 10 GHz and (b, right) 13 GHz. The simulated snowpack density is 183.4 kg/m^3, depth is 30 cm, and the snow microstructure parameter b is 1.4.

ΔTB = 20 K, which is quite large compared with TB measurement errors. Therefore, 37 GHz TB observation is promising to determine the scattering albedo of snow.

In a real application, it is rare to have simultaneous active and passive observations. The retrieval algorithm should accommodate timing differences between active and passive observations. The measurement interval refers to the time between successive measurements. For example, the AMSR-2 measurement interval is typically 2–3 days. In Figure 13, we show the estimated *a priori* scattering albedos at 10 and 13 GHz, respectively, are plotted as a function of measurement interval. Equation 6 is then applied to determine the scattering albedo by comparing passive observations with LUTs. The measurement frequency is interval ranged from 4 h (nearly simultaneous with active measurements) to 7 days. The scattering albedos determined based on the in situ measurements (the yellow curves) are regarded as a benchmark. In general, the estimated $\bar{\omega}_{10}$ and $\bar{\omega}_{13}$ from passive observations are in good agreement with the benchmark. The differences for both frequencies are smaller than 0.03. By revisiting Tables 2–4, for 2012–2013, there is a 0.04 difference for $\bar{\omega}_{10}$ and $\bar{\omega}_{13}$. The RMSE difference between the combined algorithm and the active-only algorithm is less than 5 mm and the correlation is almost same. Thus, the 0.03 difference is acceptable for the retrieval. For 13 GHz, the $\bar{\omega}_{13}$ is overestimated (0.01 bias) compared with the benchmark. The results indicate that the algorithm can tolerate a time difference (one week for the NoSREx) between active and passive meas-
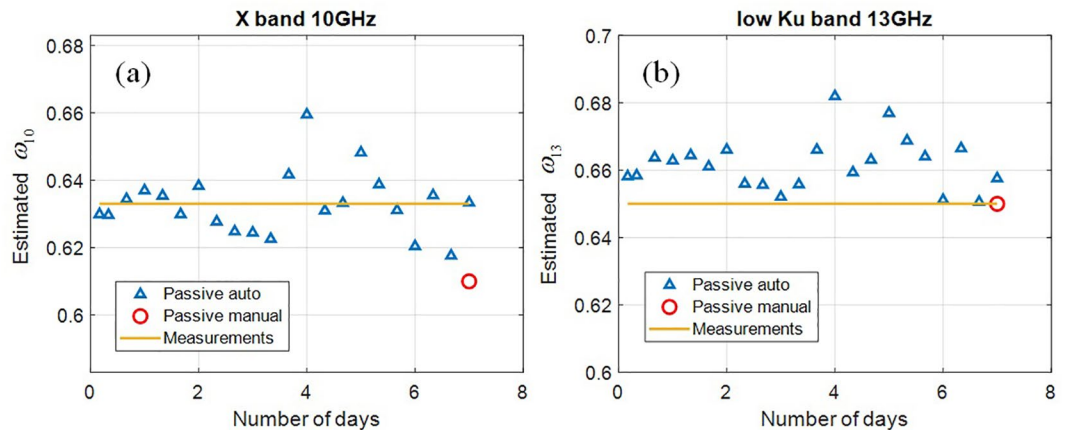

Figure 13. Estimated *a priori* scattering albedo at (a, left) 10 GHz and (b, right) 13 GHz as a function of passive measurement interval (e.g., 4 days means one passive measurement per 4 days). The red marker is the result based on passive measurements selected simultaneous with the snowpit operations. The yellow line is the result based on in situ ground measurements.

urements. Low Earth orbit measurement interval for passive observations can be once a week which still provides acceptable scattering albedos.

All the discussion and validations are based on data from the NoSREx near arctic boreal forest site in Finland. So the retrieval approach is supposed to be effective for snow in open area of boreal forest. As the original active algorithm has been validated for tundra snow (Zhu et al., 2018), the improved combine active and passive method may also work for tundra areas. Due to the bare soil assumption, the retrieval algorithm may not work for snow over sea ice. It also does not work for forest areas since forest effects have not been included in this paper. In addition, for thick snowpack (above 2 meter), backscatter at Ku bands will saturate. This may also lead to the failure of the algorithm.

As Sturm et al. (2017) pointed out, snowmelt plays an important role to generate streamflow where a seasonal snow is a key source of the water resources, and SWE becomes a critical variable to evaluate hydrological impacts driven by recent climate change (Cochand et al., 2019; Déry et al., 2009; Tague & Grant, 2009). If future remote sensing and field observations from sites with other snow types (Sturm et al., 1995) become available, the performance of the proposed active/passive algorithm should be re-calibrated and validated to demonstrate an exact SWE prediction for different snow types.

6. Conclusions

A combined active/passive retrieval algorithm is proposed and evaluated against the NoSREx data. Compared with the active-only version of the retrieval (Zhu et al., 2018), the combined active-passive algorithm provides a deterministic way to obtain an *a priori* scattering albedo by using passive observations without the need for in situ ground measurements. For the NoSREx data, the performance of this combined SWE retrieval shows promise. The *a priori* scattering albedo values estimated from passive observations are in good agreement with those from in situ measurements, and the combined algorithm achieves retrieval performance as good as the active-only algorithm. The retrieval of the combined algorithm achieves a RSME less than 27 mm and correlation coefficients above 0.68 for 2009–2010, RMSE less than 21 mm and correlation above 0.85 for 2010–2011, and RMSE less than 40 mm and correlation above 0.38 for 2012–2013. In addition, the algorithm introduces a 13 GHz radar channel that improves the robustness of the SWE retrieval. The 13 and 17 GHz backscatter is less affected by background scattering and more sensitive to the SWE. By incorporating the 13 GHz channel, the retrieval performance is enhanced and the background effects are limited.

Improvements for the combined active-passive algorithm are still needed. Although the 13 GHz channel is introduced to reduce uncertainties from background scattering, it is still challenging to characterize the snow/ground interface and compute the background scattering. Testing of the combined algorithm (with in situ ground truth) for a wider range of snow classfications (Sturm et al., 1995) than experienced during NoSREx is needed. In the absence of radar acquisitions before the snow season, existing satellite radar sensors like TerraSAR-X (X band) and Sentinel-1 (C band) could be used to obtain radar measurements at different frequencies over the study area. Those low-frequency observations might allow the removal of background scattering associated with the lower boundary by relating the low-frequency backscatter to SWE retrieval frequencies via frequency-scaling laws. Additionally, the paper describes a natural, multi-layered and heterogeneous snowpack with only a single homogeneous layer. Results showed that the single-layer model cannot account for the complex evolution of snow stratigraphy which leads to uncertainties of the SWE retrieval. A two-layer snow physics model is desirable to improve the algorithm (King et al., 2018). Furthermore, the resolution difference between active and passive microwave sensors for satellite remote sensing needs to be overcome in future studies. Another limitation of the implemented method is associated with the SWE retrieval with a bare soil assumption. Forest effects need to be further evaluated with the microwave volume scattering approach (Rott et al., 2010). With ancillary data of ground conditions and snow properties, quantitatively study uncertainties for the estimation of scattering albedo from passive observations will also be a goal for our future study.

Recent climate change has been shown to significantly alter previously stable annual water budgets—especially when snowmelt-runoff dominates the freshwater supply (Diffenbaughet al., 2015; Fowler et al., 2003; Harley et al., 2020). As noted in Sturm (2015) and Sturm et al. (2017), improved cold region hydrology is becoming more and more critical and urgent, as snowmelt-dominated water sources are shrinking. At a

global scale, a near earth orbit satellite can provide observations with a 5–10 day revisit cycle, to enhance cryospheric condition tracking. At smaller scales, the SWE retrieval algorithms presented in this paper can drive distributed land surface models across watersheds for improved streamflow prediction (Bales et al., 2006; Durand et al., 2008).

Data Availability Statement

Data sets for this research are included in this paper (Lemmetyinen et al., 2016).

References

Bales, R. C., Molotch, N. P., Painter, T. H., Dettinger, M. D., Rice, R., & Dozier, J. (2006). Mountain hydrology of the western United States. *Water Resources Research*, *42*, W08432. https://doi.org/10.1029/2005WR004387

Broxton, P. D., Van Leeuwen, W. J., & Biederman, J. A. (2019). Improving snow water equivalent maps with machine learning of snow survey and lidar measurements. *Water Resources Research*, *55*(5), 3739–3757. https://doi.org/10.1029/2018wr024146

Chang, A. T. C., Foster, J. L., & Hall, D. K. (1987). Nimbus-7 SMMR derived global snow cover parameters. *Annals of Glaciology*, *9*, 39–44. https://doi.org/10.1017/s0260305500000355

Chang, W., Ding, K. H., Tsang, L., & Xu, X. (2016). Microwave scattering and medium characterization for terrestrial snow with QCA-Mie and bicontinuous models: Comparison studies. *IEEE Transactions on Geoscience and Remote Sensing*, *54*(6), 3637–3648. https://doi.org/10.1109/TGRS.2016.2522438

Chang, W., Tan, S., Lemmetyinen, J., Tsang, L., Xu, X., & Yueh, S. H. (2014). Dense media radiative transfer applied to SnowScat and SnowSAR. *IEEE Journal of Selected Topics in Applied Earth Observations and Remote Sensing*, *7*(9), 3811–3825. https://doi.org/10.1109/JSTARS.2014.2343519

Cline, D., Elder, K., Davis, B., Hardy, J., Liston, G. E., Imel, D., et al. (2003). Overview of the NASA cold land processes field experiment (CLPX-2002). In *Microwave Remote Sensing of the Atmosphere and Environment III* (Vol. 4894, pp. 361–372). International Society for Optics and Photonics.

Cochand, M., Christe, P., Ornstein, P., & Hunkeler, D. (2019). Groundwater storage in high alpine catchments and its contribution to streamflow. *Water Resources Research*, *55*, 2613–2630. https://doi.org/10.1029/2018WR022989

Cui, Y., Xiong, C., Lemmetyinen, J., Shi, J., Jiang, L., Peng, B., et al. (2016). Estimating snow water equivalent with backscattering at X and Ku band based on absorption loss. *Remote Sensing*, *8*(6), 505. https://doi.org/10.3390/RS8060505

Derksen, C., Lemmetyinen, J., King, J., Garnaud, C., Belair, S., Lapointe, M., et al (2018). A new dual-frequency Ku-band radar mission concept for cryosphere applications. *Paper presented at 12th European Conference on Synthetic Aperture Radar Electronic Proceedings, 04–07 June, 2018. Aachen, Germany*.

Déry, S. J., Stahl, K., Moore, R. D., Whitfield, P. H., Menounos, B., & Burford, J. E. (2009). Detection of runoff timing changes in pluvial, nival, and glacial rivers of western Canada. *Water Resources Research*, *45*, W04426. https://doi.org/10.1029/2008WR006975

Diffenbaugh, N. S., Swain, D. L., & Touma, D. (2015). Anthropogenic warming has increased drought risk in California. *Proceedings of the National Academy of Sciences*, *112*(13), 3931–3936. https://doi.org/10.1073/pnas.1422385112

Ding, K. H., Xu, X., & Tsang, L. (2010). Electromagnetic scattering by bicontinuous random microstructures with discrete permittivities. *IEEE Transactions on Geoscience and Remote Sensing*, *48*(8), 3139–3151. https://doi.org/10.1109/TGRS.2010.2043953

Drinkwater, M. R., Long, D. G., & Bingham, A. W. (2001). Greenland snow accumulation estimates from satellite radar scatterometer data. *Journal of Geophysical Research*, *106*(D24), 33935–33950. https://doi.org/10.1029/2001JD900107

Durand, M., Molotch, N. P., & Margulis, S. A. (2008). Merging complementary remote sensing datasets in the context of snow water equivalent reconstruction. *Remote Sensing of Environment*, *112*(3), 1212–1225. https://doi.org/10.1016/j.rse.2007.08.010

Ficke, A. D., Myrick, C. A., & Hansen, L. J. (2007). Potential impacts of global climate change on freshwater fisheries. *Reviews in Fish Biology and Fisheries*, *17*(4), 581–613. https://doi.org/10.1007/s11160-007-9059-5

Fowler, H. J., Kilsby, C. G., & O'Connell, P. E. (2003). Modeling the impacts of climatic change and variability on the reliability, resilience, and vulnerability of a water resource system. *Water Resources Research*, *39*, 1222. https://doi.org/10.1029/2002WR001778

Hall, N. D., Stuntz, B. B., & Abrams, R. H. (2008). Climate change and freshwater resources. *Natural Resources and Environment*, *22*(3), 30–35.

Harley, G. L., Maxwell, R. S., Black, B. A., & Bekker, M. F. (2020). A multi-century, tree-ring-derived perspective of the North Cascades (USA) 2014–2016 snow drought. *Climatic Change*, *162*(1), 127–143.

Hauer, F. R., Baron, J. S., Campbell, D. H., Fausch, K. D., Hostetler, S. W., Leavesley, G. H., et al. (1997). Assessment of climate change and freshwater ecosystems of the Rocky Mountains, USA and Canada. *Hydrological Processes*, *11*(8), 903–924. https://doi.org/10.1002/(sici)1099-1085(19970630)11:8<903::aid-hyp511>3.0.co;2-7

Heino, J., Virkkala, R., & Toivonen, H. (2009). Climate change and freshwater biodiversity: Detected patterns, future trends and adaptations in northern regions. *Biological Reviews*, *84*(1), 39–54. https://doi.org/10.1111/j.1469-185x.2008.00060.x

Kelly, R. E., Chang, A. T., Tsang, L., & Foster, J. L. (2003). A prototype AMSR-E global snow area and snow depth algorithm. *IEEE Transactions on Geoscience and Remote Sensing*, *41*, 230–242. https://doi.org/10.1109/TGRS.2003.809118

Kim, E., Gatebe, C., Hall, D., Newlin, J., Misakonis, A., Elder, K., et al. (2017). NASA's SnowEx campaign: Observing seasonal snow in a forested environment. In *2017 IEEE International Geoscience and Remote Sensing Symposium (IGARSS)* (pp. 1388–1390). IEEE.

King, J., Derksen, C., Toose, P., Langlois, A., Larsen, C., Lemmetyinen, J., et al. (2018). The influence of snow microstructure on dual-frequency radar measurements in a tundra environment. *Remote Sensing of Environment*, *215*, 242–254. https://doi.org/10.1016/j.rse.2018.05.028

Leinss, S., Wiesmann, A., Lemmetyinen, J., & Hajnsek, I. (2015). Snow water equivalent of dry snow measured by differential interferometry. *IEEE Journal of Selected Topics in Applied Earth Observations and Remote Sensing*, *8*(8), 3773–3790. https://doi.org/10.1109/jstars.2015.2432031

Lemmetyinen, J., Derksen, C., Rott, H., Macelloni, G., King, J., Schneebeli, M., et al. (2018). Retrieval of effective correlation length and snow water equivalent from radar and passive microwave measurements. *Remote Sensing*, *10*(2), 170. https://doi.org/10.3390/rs10020170

Lemmetyinen, J., Derksen, C., Toose, P., Proksch, M., Pulliainen, J., Kontu, A., et al. (2015). Simulating seasonally and spatially varying snow cover brightness temperature using HUT snow emission model and retrieval of a microwave effective grain size. *Remote Sensing of Environment*, *156*, 71–95. https://doi.org/10.1016/j.rse.2014.09.016

Lemmetyinen, J., Kontu, A., Pulliainen, J., Vehviläinen, J., Rautiainen, K., Wiesmann, A., et al. (2016). Nordic snow radar experiment. *Geoscientific Instrumentation, Methods and Data Systems*, *5*, 403–415. https://doi.org/10.5194/gi-5-403-2016

Liang, D., Xu, X., Tsang, L., Andreadis, K. M., & Josberger, E. G. (2008). Multi-layer effects in passive microwave remote sensing of dry snow using dense media radiative transfer theory (DMRT) based on quasicrystalline. *IEEE Transactions on Geoscience and Remote Sensing*, *46*(11), 3663–3671. https://doi.org/10.1109/IGARSS.2007.4423024

Lievens, H., Demuzere, M., Marshall, H. P., Reichle, R. H., Brucker, L., Brangers, I., et al. (2019). Snow depth variability in the Northern Hemisphere mountains observed from space. *Nature Communications*, *10*(1), 1–12. https://doi.org/10.1038/s41467-019-12566-y

Markus, T., & Cavalieri, D. J. (1998). Snow depth distribution over sea ice in the Southern Ocean from satellite passive microwave data. *Antarctic Sea Ice: Physical Processes, Interactions and Variability*, *74*, 19–39.

Meta, A., Imbembo, E., Trampuz, C., Coccia, A., & De Luca, G. (2012). A selection of meta sensing airborne campaigns at L-, X- and Ku band. *EUSAR 2012; 9th European Conference on Synthetic Aperture Radar, Nuremberg, Germany* (pp. 414–417).

National Research Council. (2007). *Earth science and applications from space: National imperatives for the next decade and beyond*. National Academies Press.

Oh, Y., Sarabandi, K., & Ulaby, F. T. (1992). An empirical model and an inversion technique for radar scattering from bare soil surfaces. *IEEE Transactions on Geoscience and Remote Sensing*, *30*(2), 370–381. https://doi.org/10.1109/36.134086

Pan, J., Durand, M. T., Vander Jagt, B. J., & Liu, D. (2017). Application of a Markov Chain Monte Carlo algorithm for snow water equivalent retrieval from passive microwave measurements. *Remote Sensing of Environment*, *192*, 150–165. https://doi.org/10.1016/j.rse.2017.02.006

Pettinato, S., Santi, E., Brogioni, M., Paloscia, S., Palchetti, E., & Xiong, C. (2013). The potential of COSMO-SkyMed SAR images in monitoring snow cover characteristics. *IEEE Geoscience and Remote Sensing Letters*, *10*(1), 9–13. https://doi.org/10.1109/LGRS.2012.2189752

Proksch, M., Mätzler, C., Wiesmann, A., Lemmetyinen, J., Schwank, M., Löwe, H., & Schneebeli, M. (2015). MEMLS3&a: Microwave Emission Model of Layered Snowpacks adapted to include backscattering. *Geoscientific Model Development*, *8*, 2611–2626. https://doi.org/10.5194/gmd-8-2611-2015

Pulliainen, J., & Hallikainen, M. (2001). Retrieval of regional snow water equivalent from space-borne passive microwave observations. *Remote Sensing of Environment*, *75*(1), 76–85. https://doi.org/10.1016/s0034-4257(00)00157-7

Rott, H., Yueh, S. H., Cline, D. W., Duguay, C., Essery, R., Haas, C., et al. (2010). Cold regions hydrology high-resolution observatory for snow and cold land processes. *Proceedings of the IEEE*, *98*(5), 752–765. https://doi.org/10.1109/JPROC.2009.2038947

Saberi, N., Kelly, R., Flemming, M., & Li, Q. (2020). Review of snow water equivalent retrieval methods using spaceborne passive microwave radiometry. *International Journal of Remote Sensing*, *41*(3), 996–1018. https://doi.org/10.1080/01431161.2019.1654144

Shah, R., Xu, X., Yueh, S., Chae, C. S., Elder, K., Starr, B., & Kim, Y. (2017). Remote sensing of snow water equivalent using P-band coherent reflection. *IEEE Geoscience and Remote Sensing Letters*, *14*(3), 309–313. https://doi.org/10.1109/lgrs.2016.2636664

Shi, J., & Dozier, J. (2000). Estimation of snow water equivalence using SIR-C/X-SAR. II. Inferring snow depth and particle size. *IEEE Transactions on Geoscience and Remote Sensing*, *38*(6), 2475–2488. https://doi.org/10.1109/36.885196

Staudinger, M., Stahl, K., & Seibert, J. (2014). A drought index accounting for snow. *Water Resources Research*, *50*, 7861–7872. https://doi.org/10.1002/2013WR015143

Sturm, M. (2015). White water: Fifty years of snow research in WRR and the outlook for the future. *Water Resources Research*, *51*, 4948–4965. https://doi.org/10.1002/2015WR017242

Sturm, M., Goldstein, M. A., & Parr, C. (2017). Water and life from snow: A trillion dollar science question. *Water Resources Research*, *53*, 3534–3544. https://doi.org/10.1002/2017WR020840

Sturm, M., Holmgren, J., & Liston, G.E. (1995). A seasonal snow cover classification system for local to global applications. *Journal of Climate*, *8*, 1261–1283. https://doi.org/10.1175/1520-0442(1995)008<1261:ASSCCS>2.0.CO;2

Tague, C., & Grant, G. E. (2009). Groundwater dynamics mediate low-flow response to global warming in snow-dominated alpine regions. *Water Resources Research*, *45*, W07421. https://doi.org/10.1029/2008WR007179

Tan, S., Chang, W., Tsang, L., Lemmetyinen, J., & Proksch, M. (2015). Modeling both active and passive microwave remote sensing of snow using dense media radiative transfer (DMRT) theory with multiple scattering and backscattering enhancement. *IEEE Journal of Selected Topics in Applied Earth Observations and Remote Sensing*, *8*(9), 4418–4430. https://doi.org/10.1109/JSTARS.2015.2469290

Thompson, A., & Kelly, R. (2019). Observations of a coniferous forest at 9.6 and 17.2 GHz: Implications for SWE retrievals. *Remote Sensing*, *11*(1), 6. https://doi.org/10.3390/rs11010006

Tsang, L., Kong, J. A., & Ding, K. H. (2004). *Scattering of electromagnetic waves: Theories and applications* (Vol. 27). John Wiley & Sons.

Ulaby, F. T., & Stiles, W. H. (1980). The active and passive microwave response to snow parameters: 2. Water equivalent of dry snow. *Journal of Geophysical Research*, *85*(C2), 1045–1049. https://doi.org/10.1029/jc085ic02p01045

Xiong, C., & Shi, J. (2017). The potential for estimating snow depth with QuikScat data and a snow physical model. *IEEE Geoscience and Remote Sensing Letters*, *14*(7), 1156–1160. https://doi.org/10.1109/LGRS.2017.2701808

Xu, X., Tsang, L., & Yueh, S. (2012). Electromagnetic models of co/crosspolarization of bicontinuous/DMRT in radar remote sensing of terrestrial snow at X- and Ku-band for CoReH2O and SCLP applications. *IEEE Journal of Selected Topics in Applied Earth Observations and Remote Sensing*, *5*(3), 1024–1032. https://doi.org/10.1109/JSTARS.2012.2190719

Zhu, J., Tan, S., King, J., Derksen, C., Lemmetyinen, J., & Tsang, L. (2018). Forward and inverse radar modeling of terrestrial snow using SnowSAR data. *IEEE Transactions on Geoscience and Remote Sensing*, *56*(12), 7122–7132. https://doi.org/10.1109/TGRS.2018.2848642